RESEARCH ARTICLE

Photonic crystal based photoelectrochemical cell for solar fuels

Xiwen Zhang [ORCID] | Sajeev John

Department of Physics, University of
Toronto, Toronto, Ontario, Canada

Correspondence
Xiwen Zhang, Department of Physics,
University of Toronto, 60 Saint George
Street, Toronto, Ontario M5S 1A7, Canada.
Email: xiwen@mail.ustc.edu.cn
Sajeev John, Department of Physics, University of Toronto, 60 Saint George Street,
Toronto, Ontario M5S 1A7, Canada.
Email: john@physics.utoronto.ca

Abstract
The solar fuel production efficiency of photoelectrochemical cells based on TiO_2 is primarily limited by the low optical absorption coefficient and concomitant long penetration depth of visible light compared with the minority charge carrier diffusion length. A TiO_2 photoelectrode consisting of a slanted conical-pore photonic crystal immersed in water and integrated on a reflective back-contact is proposed to reduce the light penetration depth by more than 10 times and branch the electron and hole transports into dimensions matching their diffusion lengths. This brings the photoelectrolytic process into the high-efficiency operating regime. The maximum achievable photocurrent density for a lightly doped TiO_2 with the imaginary part of the dielectric constant 0.01 in the visible range reaches 7.65 mA cm^{-2}.

KEYWORDS
light harvesting, photoelectrochemical cell, photonic crystal, solar fuel

Chemical storage of solar energy is an important candidate for economically and sustainably mitigating global energy problems and environmental pollution. Unlike photovoltaics[1] that involves immediate usage of solar power, photogenerated electron-hole pairs in a semiconductor migrate to available surfaces to drive chemical reactions through which energy can be stored for later use. Solar fuel production, such as water-splitting, often relies on photoelectrochemical (PEC) cells based on wide-band semiconductors like TiO_2 due to its high photochemical activity, physical and chemical stability in water, abundancy, and nontoxicity.[2–4] However, the wide electronic bandgap $\sim$ 3.2 eV of TiO_2 critically limits its sunlight harvesting to the ultraviolet (UV) part of the spectrum, which contains only $\sim$ 4% of the solar irradiance energy.

Extensive efforts have been devoted to the bandgap engineering of TiO_2 by doping with non-metal anions and a wide range of metal cations,[5,6] as well as the co-doping of their various combinations.[7,8] These modifications change both the optical and the transport properties of TiO_2. While the visible light absorptivity is typically increased by induced defect states inside the electronic bandgap, the photocatalytic efficiency and material stability may deteriorate since defect sites act as extrinsic charge recombination centers,[8–10] and excess carriers can reduce space charge region (SCR).[11]

Intrinsic charge carrier recombination in TiO_2 occurs largely on surface defect sites. These surface defects, on the other hand, can be important for energy-harvesting redox photochemical reactions. Therefore, a spatial separation of the photogenerated electrons and holes is crucial to reduce unwanted surface recombination while exploiting redox reaction centers. This is enabled by the electronic band bending of TiO_2 near the semiconductor-electrolyte

interface.[12] The upward band bending from the bulk to the surface creates a SCR of thickness W in which the electrons are pulled into the bulk and holes are pushed toward the surface, consequently quenching the recombination. Outside the SCR, electrons and holes can diffuse freely over their respective diffusion lengths L_n and L_p before recombination occurs. Since $L_p \ll L_n$ in TiO$_2$,[13–17] charges photogenerated within a distance of L_p of a TiO$_2$-water interface can be efficiently collected.

There are four critical lengths scales determining the PEC cell efficiency, namely, SCR thickness W, hole diffusion length L_p, optical absorption length l_{abs}, and physical thickness of the electrode h. The optical absorption length, also called light penetration depth, is defined through the Beer-Lambert law as the depth at which the light intensity falls to 37% of its value at the entrance inside the bulk. Since l_{abs} is a frequency dependent intrinsic bulk property, we introduce a critical height h_c (also called the optical penetration depth) representing the height of the electrode for which the average absorptivity [see Equation (3)] in a spectral region reaches 63%.

For planar film photoelectrodes, the efficient charge carrier generation requires $h_c \lesssim h$, while the efficient electron-hole separation and collection requires $h \lesssim W + L_p$.[18] If $h \ll W$ the band bending effect is degraded, whereas if $h \gg W + L_p$ the photogenerated electrons and holes recombine before being collected.[17,19] Since the solar photon number in the 400 to 550 nm wavelength region is six times as many as in the UV region, it is essential to bring h_c in this entire UV to visible range close to the regime of $W + L_p$. However, in TiO$_2$, the typical length scales are $W \sim 50$ nm[11,16,20] and $L_p \sim 10$–300 nm,[13–16] while $l_{abs} = 20$ μm for a 470 nm wavelength photon in a lightly doped TiO$_2$ with the imaginary part of the dielectric constant 0.01. There is at least two orders of magnitude difference between the absorption length and the space charge thickness and/or hole diffusion length.

To bring the photoelectrolytic process into the high-efficiency operating regime, we propose to use wave-interference-based light trapping in a TiO$_2$ electrode consisting of a slanted conical-pore photonic crystal (PC).[21] The strong light confinement ability of this PC due to wave interference, in a spectrally dense distribution of slow-light modes (photonic modes with group velocities much smaller than the speed of light in a structureless medium), enables the efficient light harvesting over the required UV to visible range in a weakly absorbing material, in a way not possible in other non-periodic nanostructures such as nanowires and nanotubes.[22] Various PC architectures allow a reduction of h_c by more than an order of magnitude, without introducing bulk recombination centers, to the photocatalyst to fulfill $h_c < h$. They also introduce TiO$_2$-water interfaces throughout the interior of the pho-
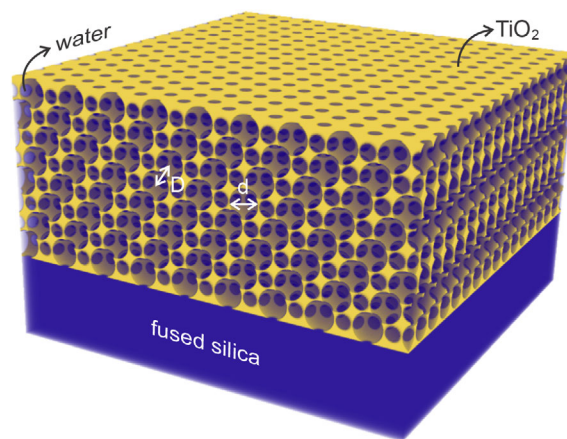

FIGURE 1 Illustration of an eight-layer TiO$_2$ face-centered cubic inverse opal PC with $d/D = 1.056$ on a fused silica substrate in water

toelectrode. This enables efficient carrier collection even for $h \gg W + L_p$ (provided that $h \lesssim W + L_n$), by branching electrons and holes into dimensions with scales matching their diffusion lengths. For the slanted conical- pore PC (Figure 3) the requirement of efficient photoelectrolysis changes to $a \lesssim W + L_p$ and $h \lesssim W + L_n$ where a is the lattice constant, because the holes need only drift and/or diffuse at most one lattice constant to reach an available surface, whereas electrons need to drift and/or diffuse at most by the entire height of the PC to be collected by the bottom contact. For the inverse opal PC (Figure 1), on the other hand, the requirement on h becomes $h \ll W + L_n$ since there is no straight-line path to the bottom contact.

In the past two decades, the inverse opal PC (Figure 1) has been experimentally used in dye-sensitized solar cells[23] and photocatalysis.[24] Some of the pertinent works were devoted to the PEC hydrogen production[25–30] with sensitized TiO$_2$. However, enhancement of photoreactivity due to PC light trapping is insignificant or absent compared with the increase resulting from sensitizer loading given the ample porosity and the large interior surface area of the inverse opal structure.[26,29] This increase sometimes relies on an environmentally hazardous sacrificial reagent for hole scavenging prior to recombination.[25,26,28,29,31]

The widely-studied inverse opal architecture is not ideal for PEC solar fuel generation for three reasons. Firstly, the bottom-up fabrication approach based on the infiltration of a colloidal opal crystal template suffers from the incomplete backfilling, volume shrinkage, and geometrical cracking.[32,33] These deformations disrupt high-frequency, slow-light modes of the inverse opal. The intact slow-light modes occur on either side of the fundamental stop gap.[24] These low frequency slow-photon modes in the inverse opal PC have very limited light
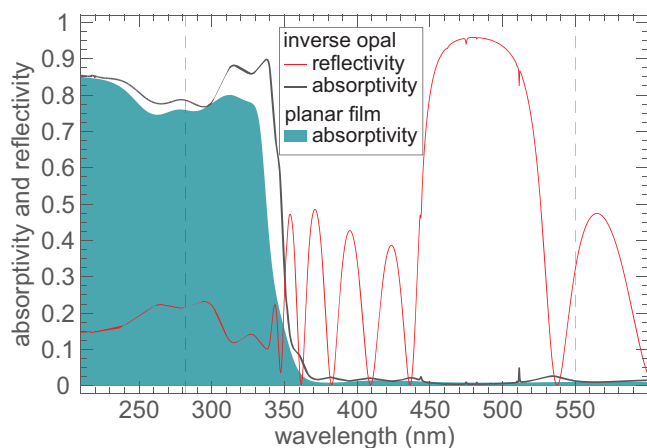
FIGURE 2 Absorptivity (black solid line) and reflectivity (red thin solid line) spectra of an eight-layer (height $h = 1.287\,\mu m$) inverse opal PC with $D = 190$ nm and $d = 200.6$ nm, and the absorptivity spectrum of a planar TiO$_2$ film with equivalent bulk thicknesses $h_{TiO_2} = 230$ nm (sea-green filled color) under normal incidence. Both structures are placed on fused silica glass substrates in aqueous environments. The vertical dash lines encompass the spectral region of $\lambda \in [282, 550]$ nm

trapping ability and do not significantly reduce the optical penetration depth (for example, see Figure 2 and Table 1). Recently it has been suggested that much stronger light trapping can be achieved in higher order photonic bands in high-quality inverse opals.[34] Secondly, the morphology of the inverse opal PC is disadvantageous to charge carrier separation and transport. The narrow and tortuous necks of the scaffold degrade the SCR. These narrow necks of the TiO$_2$ backbone are much less than $D/2$, where D is the opal center-to-center distance (see Figure 1).[24,35–37] For $D = 190$ nm, the TiO$_2$ wall thickness, depending on the location, is only a few nanometers to a few tens of nanometers, smaller than the typical SCR thickness W. A small increase of D, however, reduces the PC

light trapping effect due to the shift of the fundamental-band-edge slow-light modes. Typically, the inverse opal structure degrades the band bending of TiO$_2$. Indeed, the band bending is well known to decrease with the size of semiconductor particles, becoming negligibly small for particles much smaller than the SCR thickness.[38–40] In this case, it is impossible to spatially separate the electrons and holes. Moreover, in such a thin scaffold wall, charge carriers can easily tunnel from the bulk to the surface for rapid recombination. In an inverse opal, the effect of any residual band bending may be to trap electrons in the bulkier regions of the TiO$_2$ wall, behaving like a potential well, while blocking their flow in the photoanode. Untrapped electrons need to travel a tortuous path much longer than the PC thickness to be collected because of curvy morphology. In addition to insufficient electron conducting paths, the situation is aggravated by the poor interfacial contact with the bottom of the electrode.[41] In principle, a conformal partial metallic frame[42] may help the electron transport to the non-aqueous contact, but it decreases light absorptivity and increases ohmic loss. Indeed, the photocatalytic reactivity of $\lesssim 100$ nm-sized catalyst particles was found to decrease with size reduction.[43–45] Thirdly, the inner porous structure of inverse opal PC easily traps oxygen gas bubbles inside the photoelectrode,[46,47] impeding the chemical reacants from reaching the reaction sites and eventually limiting the reaction rate.

An ideal PC photoelectrode architecture requires robust, dense and broadband slow-light modes for light harvesting, at the same time preserve the electronic band bending and SCR for electron and hole separation, provide unobstructed conducting paths for charge diffusion and collection, and present easily accessible open TiO$_2$-water interfaces for fast adsorption and desorption of reactants and products on the catalyst. In this paper, we propose a slanted conical-pore PC structure[48] integrated on a

TABLE 1 The figures of merit of PEC cell in the UV and visible spectral ranges for the photoelectrodes of eight-layer inverse opal PC on glass and slanted conical-pore PC on mirror

Architecture	PC parameters (nm)				MAPD (mA cm^{-2})				ζ			A_{avg}	t_j (μm)	t_A (μm)
			h	h_{TiO_2}	UV	Vis	UV-vis	UV-vis'	UV	Vis	UV-vis		UV-vis	
Inverse opal on glass	D	d												
	190	200.6	1287	230.0	0.333	0.105	0.438	0.368	1.49	1.19	1.40	0.337	0.403	0.88
	a	r												
Slanted conical-pore on mirror	350	201.25	700	462.6	0.683	2.17	2.86	1.16	2.39	11.94	6.10	0.561	6.54	9.76
	350	175	700	516.7	0.697	2.44	3.14	1.21	2.37	11.65	6.23	0.568	7.48	10.21
	350	201.25	1300	859.1	0.837	3.18	4.01	1.75	2.43	9.51	5.91	0.653	10.77	16.92
	350	175	1300	959.7	0.777	3.33	4.10	1.48	2.17	8.94	5.63	0.631	11.15	14.85

UV, Vis, UV-vis, and UV-vis' stand for the spectral regions of $\lambda \in [282, 400]$ nm, $[400, 550]$ nm, $[282, 550]$ nm and $[282, 450]$ nm, respectively. h and h_{TiO_2} are the thicknesses of the PC and the equivalent bulk, while t_j (t_A) is the thickness of the TiO$_2$ planar film deposited on a fused silica substrate demonstrating the same MAPD (A_{avg}) as the PC on a substrate does in the specified spectral range.

reflective bottom contact to fulfill these conditions and improve the efficiency of solar fuel photoproduction by an order of magnitude.

In contrast to the heavy-doping approach for light harvesting, we assume very slightly doped TiO_2 to introduce nonvanishing visible light absorption without deteriorating the charge transport properties through excess recombination centers. The optical model of TiO_2 is based on the experimental data of the single crystal anatase[49] by averaging out the anisotropy, with an extension into the 400 to 550 nm range of the imaginary part of the dielectric constant, which we set to a constant value of 0.01[50] (see also the Supporting Information). Light absorptivities are numerically simulated by solving Maxwell's equation in normal incidence using the finite-difference time-domain method, with 70 mesh grids per lattice constant of the PC. To evaluate the efficiency of light trapping for solar fuel production, we utilize the figure of merit given by the maximum achievable photocurrent density (MAPD) in a wavelength range $\lambda \in [\lambda_1, \lambda_2]$, in which each absorbed solar photon produces one electron-hole pair:

$$\text{MAPD} = \frac{e}{hc} \int_{\lambda_1}^{\lambda_2} A(\lambda) I_s(\lambda) \lambda d\lambda. \quad (1)$$

Here, e is the electron charge, h is the Planck constant, c is the speed of light in vacuum, A is the structure-dependent absorptivity including the effect of light trapping, and I_s is the AM1.5G solar irradiance spectrum. In order to highlight the role of PC morphology, we define an MAPD enhancement factor relative to a bulk planar TiO_2 film of the same mass[34]:

$$\zeta = \text{MAPD}_{PC} / \text{MAPD}_{bulk}. \quad (2)$$

Here, MAPD_{PC} is that of the PC (on fused silica glass or mirror substrate) and MAPD_{bulk} is that of a planar film of the same mass on a glass substrate. The film thickness that matches the TiO_2 mass of the PC is called equivalent bulk thickness h_{TiO_2}. In addition, we define the average light absorptivity as

$$A_{avg} = \frac{1}{f_1 - f_2} \int_{f_2}^{f_1} A(f) df, \quad (3)$$

where $[f_2, f_1]$ is the frequency range of interest.

We first investigate the light trapping effect of the inverse opal PC with typical structural parameters found in photocatalysis experiments using nonsensitized TiO_2.[51] In these experiments, the photonic modes near the fundamental optical stop gap are aligned with the edge of the electronic band 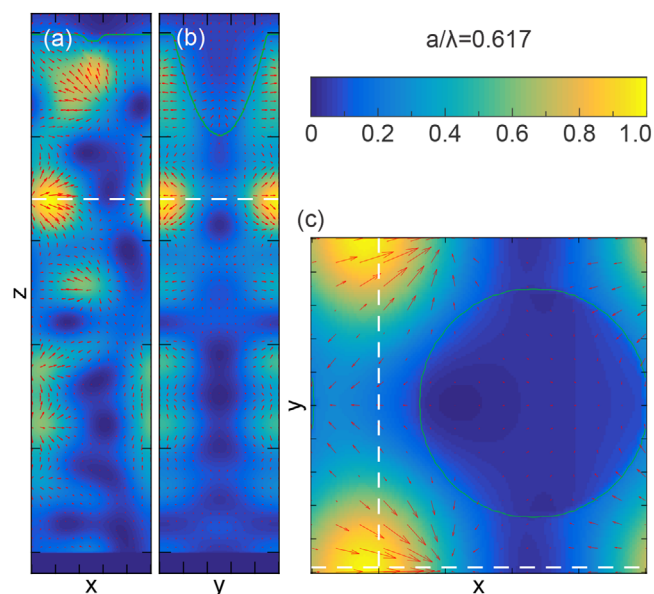gap in order to slightly extend (over a very small spectral range) the optical absorption to longer wavelength. The PCs are either deposited on conductive (as in solar cells) or nonconductive glasses. We consider an eight-layer face-centered cubic inverse opal PC on a fused silica glass substrate, with sphere center-to-center distance $D = 190$ nm and sphere diameter $d = 200.6$ nm (Figure 1). The volume fraction of TiO_2 is 17.9%. This places the short-wavelength (blue-shifted) side of the fundamental photonic stop gap around the edge of the electronic band gap. The overall height of the PC is $h = 1.287\,\mu m$, and the equivalent bulk thickness is $h_{TiO_2} = 230$ nm. The absorptivity and reflectivity spectra for both the TiO_2 PC on glass and the TiO_2 planar film on glass are shown in Figure 2.

From Figure 2 it is seen that the light absorptivity of the inverse opal PC on glass is slightly better than the planar film in the vicinity of the TiO_2 conduction band. As listed in Table 1, the MAPD and its enhancement factor ζ are 0.438 mA cm^{-2} and 1.4, respectively, over the spectral region $\lambda \in [282, 550]$ nm. Experimentally, pristine TiO_2 inverse opal PCs, made from ~ 300 nm sphere-diameter template opals, with $h \sim 8$ and 2 μm demonstrated photocurrent densities ~ 0.017 and 0.25 mA cm^{-2}, respectively, at 0 volts potential with respect to the Ag/AgCl reference electrodes in sacrificial electrolytes.[25,26] Photoelectrodes of thicknesses 5 to 6 μm composed of inverse opal PC[30] and PC deposited on TiO_2 nanorods[27] exhibited photocurrent densities around 0.6 mA cm^{-2} at ~ 1 volt potential with respect to the reversible hydrogen electrode. So far the experimentally demonstrated inverse-opal light trapping and harvesting effect is far below the actual potential of wave-interference-based light trapping in an optimally designed PC. For the inverse opal utilizing slow-light modes near the fundamental stop gap in Figure 2, the MAPD in the visible 400 to 550 nm range is only increased by $\zeta = 1.19$ times relative to the planar film. A dramatic improvement is possible using a photoelectrode made of slanted conical-pore PC on mirror architecture, as we describe below.
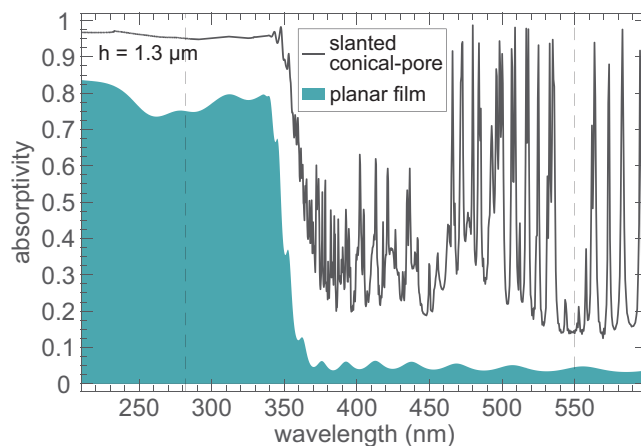
Our optimized PC is composed of a square lattice array of slanted conical pores (see Figure 3), characterized by the lattice constant a, base radius r, and height h. This photoelectrode is placed on a perfectly reflecting metal. This architecture exhibits remarkably improved light trapping and harvesting ability compared with the inverse opal due to parallel-to-interface-refraction (PIR) of incident light into a wider band of slow-light modes[50,52–55] (see Figure 4). A second distinctive feature is the improved anti-reflection due to the intrinsic gradient refractive index profile.[48] A third improvement to light trapping is the closure of the transmission channel by the mirror.[52,55] The mirror substrate also acts as an electron collector, preferably with an Ohmic junction and suitable band bending[56,57] to facilitate electron flow to a counter
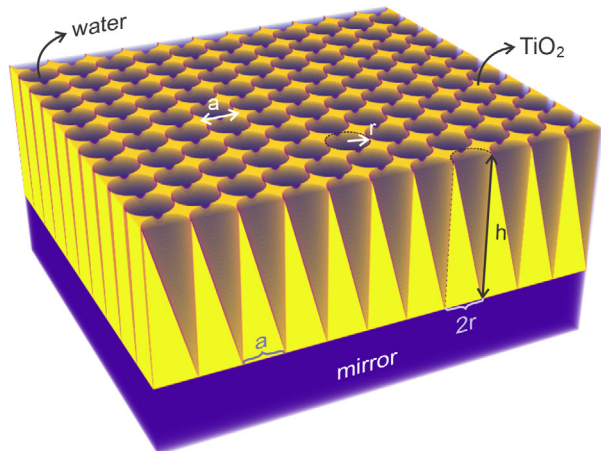
FIGURE 3 Illustration of a TiO$_2$ slanted conical-pore PC of height h with $r/a = 0.5$ on a reflective substrate in water. Each cone has one vertical line along its surface, so the cone center axis is slightly off-normal. This provides better light trapping than the corresponding vertical-axis conical-pore PC

FIGURE 5 Absorptivity spectra of a slanted conical-pore PC on a mirror substrate with $a = 350$ nm, $r = 175$ nm and $h = 1.3$ µm (black solid line), compared with a planar TiO$_2$ film of equivalent bulk thicknesses $h_{TiO_2} = 959.7$ nm on a fused silica substrate (sea-green filled color). Both spectra are for normal incidence and both structures are immersed in water

FIGURE 4 Distributions of electromagnetic energies ($\mathbf{E}^* \cdot \mathbf{D} + \mathbf{H}^* \cdot \mathbf{B})/2$ (color map) and Poynting vectors Re$\{\mathbf{E}^* \times \mathbf{H}\}$ (red arrows) in arbitrary units in one unit cell under normal incidence light at the frequency $a/\lambda = 0.617$ of a slanted conical-pore PC on a reflective back-contact in water with $r/a = 0.5$ and $h/a = 4.3$. The green contours outline the TiO$_2$-water interfaces. The refractive index of TiO$_2$ is taken to be 2.25. The positions of longitudinal and transverse cuts are indicated by the white dashed lines. The normal incident light excites PIR slow-light modes with energies concentrating in the absorptive catalyst and Poynting vectors lying in the (practically infinite) transverse plane of the photoelectrode. This enormously increases the optical path length and the optical dwell time. The focusing of energy into high intensity spots within TiO$_2$ also enhances the light-matter interaction strength

electrode placed elsewhere in the aqueous background. As an example, the optical absorptivity spectrum of a slanted conical-pore PC photoelectrode in water with $a = 350$ nm, $r = 175$ nm, and $h = 1.3$ µm is given in Figure 5 and compared with a planar 959.7 nm-thick TiO$_2$ film of the same active volume on a fused silica substrate.

In the spectral region of $\lambda \in [282, 550]$ nm, the MAPD for a structure of height $h = 1.3$ µm reaches 4.10 mA cm^{-2} (with the enhancement factor $\zeta = 5.63$) as shown in Figure 5 (see the Supporting Information for its spatial contributions). This is 9.4 times of that in the inverse opal on glass structure with the same PC height (see Table 1). This improvement is attributed to the broadband, densely distributed, highly absorptive slow-light resonances across the entire UV to visible spectral range, as shown in Figure 4 and 5. Especially, in the visible range of $\lambda \in [400, 550]$ nm, the MAPD is 3.33 mA cm^{-2} in the slanted conical-pore PC on mirror. This is 31.7 times of that in the inverse opal PC on glass, of the same overall height. More examples are summarized in Table 1.

From the electronics perspective, the slanted conical-pore PC preserves the vital SCR for charge-carrier separation near the TiO$_2$-water interface. In addition, the electron conduction path to the bottom contact is more straightforward than in the inverse opal PC. Clearly, the slanted conical-pore PC on mirror photoelectrode not only significantly enhances the solar light harvesting but also dramatically improves the charge carrier separation and collection.

The reduction of the photoelectrode critical height h_c (light penetration depth) by using a slanted conical-pore PC on mirror is evident by the fact that to achieve the same light absorption would require a much thicker TiO$_2$
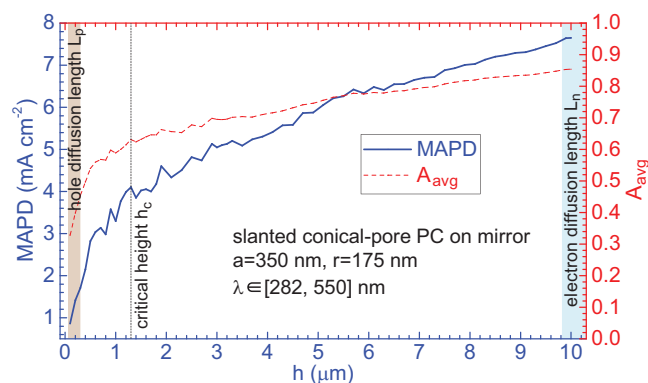
FIGURE 6 The maximum achievable photocurrent density (blue solid line) and average absorptivity (red dashed line) for a slanted conical-pore PC on a mirror substrate in water with $a = 350\,\text{nm}, r/a = 0.5$. The light brown and cyan colors indicate a plausible range of the hole and electron diffusion lengths, respectively, and the short dashed vertical line marks the PC critical height of 1.3 μm

planar film. For the case of $a = 350$ nm, $r = 175$ nm, and $h = 1.3$ μm in Table 1, $A_{\text{avg}} = 63.1\%$ in the $\lambda \in$ [282, 550] nm range, corresponding to h_c. The same average absorptivity requires a critical height of 14.85 μm of a planar film on glass. This is 11.4 times of the critical height and 15.5 times the equivalent bulk thickness of the slanted conical-pore photoelectrode.

As discussed above, the requirements of high efficiency for our slanted conical-pore photoelectrode are $a \lesssim W + L_p$ and $h_c \lesssim h \lesssim W + L_n$, rather than $h_c \lesssim h \lesssim W + L_p$ for the conventional planar photoelectrode. In TiO$_2$ $L_p \sim 10$–300 nm[13–16] and $L_n \sim 10$ μm.[17] Our improved PC relaxes the requirement on the electrode height, h, by two orders of magnitude. In Figure 6 we show that the MAPD can be increased to 7.65 mA cm^{-2} at $h = 10$ μm.

In summary, we propose a dramatically improved TiO$_2$ photoelectrode architecture consisting of slanted conical-pore PC on mirror. This substantially increases light harvesting efficiency and promotes the photogenerated electron-hole pair separation and collection in a PEC cell for solar fuel production.

Structures similar to our slanted conical-pore PC have been fabricated in silicon using plasma etching[58] and wet etching[59,60] methods. The silicon parabolic-pore PC of lattice constant 1.2 μm[58] has shown considerable light trapping and absorption enhancement. A slanted version of this structure[61] can be achieved by tilting the sample during the plasma etching process. Silicon inverted-pyramid PCs of periodicity 500 to 1500 nm[59,60] have shown comparable light trapping.[62] These illustrations offer compelling evidence that similar light harvesting enhancements can be realized for TiO$_2$ in water for solar fuel production.

Quantum dots and metallic nanoparticles can be loaded onto our TiO$_2$ PC for additional enhancement of light absorptivity and charge carrier separation.[25–30] The surface area can also be further increased,[63] if demanded, by introducing ~ 10–100 nm length TiO$_2$ nanowires on the inner surfaces of the conical pores. This is analogous to the silicon-TiO$_2$ nanotree[64] used in earlier water-splitting studies. This may further enhance light harvesting in TiO$_2$ and chemical reactivity at the aqueous interface (see the Supporting Information for more discussions).

We hope our numerical demonstration of order-of-magnitude enhancement in photocatalytic current generation will inspire future experimental studies in this unexplored path to efficient solar fuel production.

CONFLICT OF INTEREST
The authors declare no conflict of interest.

ORCID
Xiwen Zhang https://orcid.org/0000-0003-3084-7504

REFERENCES
1. S. Bhattacharya, S. John, *APL Photonics* **2020**, *5*, 020902.
2. A. Fujishima, K. Honda, *Nature* **1972**, *238*, 37.
3. A. Fujishima, X. Zhang, D. A. Tryk, *Surf. Sci. Rep.* **2008**, *63*, 515.
4. J. Schneider, M. Matsuoka, M. Takeuchi, J. Zhang, Y. Horiuchi, M. Anpo, D. W. Bahnemann, *Chem. Rev.* **2014**, *114*, 9919.
5. M. K. Nowotny, L. R. Sheppard, T. Bak, J. Nowotny, *J. Phys. Chem. C* **2008**, *112*, 5275.
6. R. Shwetharani, M. Sakar, C. A. N. Fernando, V. Binas, R. G. Balakrishna, *Catal. Sci. Technol.* **2019**, *9*, 12.
7. W. Zhu, X. Qiu, V. Iancu, X.-Q. Chen, H. Pan, W. Wang, N. M. Dimitrijevic, T. Rajh, H. M. Meyer III, M. P. Paranthaman, G. M. Stocks, H. H. Weitering, B. Gu, G. Eres, Z. Zhang, *Phys. Rev. Lett.* **2009**, *103*, 226401.
8. Y. Gai, J. Li, S.-S. Li, J.-B. Xia, S.-H. Wei, *Phys. Rev. Lett.* **2009**, *102*, 036402.
9. W. Mu, J.-M. Herrmann, P. Pichat, *Catal. Lett.* **1989**, *3*, 73.
10. M. Radecka, M. Rekas, A. Trenczek-Zajac, K. Zakrzewska, *J. Power Sources* **2008**, *181*, 46.
11. H. Xu, S. Ouyang, L. Liu, P. Reunchan, N. Umezawa, J. Ye, *J. Mater. Chem. A* **2014**, *2*, 12642.
12. Z. Zhang, J. T. Yates, *Chem. Rev.* **2012**, *112*, 5520.
13. A. K. Ghosh, H. P. Maruska, *J. Electrochem. Soc.* **1977**, *124*, 1516.
14. P. Salvador, *J. Appl. Phys.* **1984**, *55*, 2977.
15. L. Peraldo Bicelli, G. Razzini, C. Malitesta, L. Sabbatini, P. G. Zambonin, *Sol. Energy Mater.* **1986**, *13*, 25.
16. S. K. Poznyak, V. V. Sviridov, A. I. Kulak, M. P. Samtsov, *J. Electroanal. Chem.* **1992**, *340*, 73.
17. W. H. Leng, P. R. F. Barnes, M. Juozapavicius, B. C. O'Regan, J. R. Durrant, *J. Phys. Chem. Lett.* **2010**, *1*, 967.

18. W. W. Gärtner, *Phys. Rev.* **1959**, *116*, 84.

19. J. Li, N. Wu, *Catal. Sci. Technol.* **2015**, *5*, 1360.

20. M. Takahashi, K. Tsukigi, T. Uchino, T. Yoko, *Thin Solid Films* **2001**, *388*, 231.

21. S. John, *Phys. Rev. Lett.* **1987**, *58*, 2486.

22. K. Shankar, J. I. Basham, N. K. Allam, O. K. Varghese, G. K. Mor, X. Feng, M. Paulose, J. A. Seabold, K.-S. Choi, C. A. Grimes, *J. Phys. Chem. C* **2009**, *113*, 6327.

23. S. Nishimura, N. Abrams, B. A. Lewis, L. I. Halaoui, T. E. Mallouk, K. D. Benkstein, J. van de Lagemaat, A. J. Frank, *J. Am. Chem. Soc.* **2003**, *125*, 6306.

24. J. I. L. Chen, G. von Freymann, S. Y. Choi, V. Kitaev, G. A. Ozin, *Adv. Mater.* **2006**, *18*, 1915.

25. C. Cheng, S. K. Karuturi, L. Liu, J. Liu, H. Li, L. T. Su, A. I. Y. Tok, H. J. Fan, *Small* **2012**, *8*, 37.

26. K. Kim, P. Thiyagarajan, H.-J. Ahn, S.-I. Kim, J.-H. Jang, *Nanoscale* **2013**, *5*, 6254.

27. X. Zhang, Y. Liu, S.-T. Lee, S. Yang, Z. Kang, *Energy Environ. Sci.* **2014**, *7*, 1409.

28. C.-Y. Cho, S. Lee, J. Lee, D. C. Lee, J. H. Moon, *J. Mater. Chem. A* **2014**, *2*, 17568.

29. J. Lee, C.-Y. Cho, D. C. Lee, J. H. Moon, *RSC Adv.* **2016**, *6*, 8756.

30. R. Boppella, S. T. Kochuveedu, H. Kim, M. J. Jeong, F. M. Mota, J. H. Park, D. H. Kim, *ACS Appl. Mater. Interfaces* **2017**, *9*, 7075.

31. H. Zhang, C. Cheng, *ACS Energy Lett.* **2017**, *2*, 813.

32. J. E. G. J. Wijnhoven, L. Bechger, W. L. Vos, *Chem. Mater.* **2001**, *13*, 4486.

33. J. Yu, J. Lei, L. Wang, J. Zhang, Y. Liu, *J. Alloys Compd.* **2018**, *769*, 740.

34. X. Zhang, S. John, *J. Mater. Chem. A* **2020**, *8*, 18974.

35. J. S. King, E. Graugnard, C. J. Summers, *Adv. Mater.* **2005**, *17*, 1010.

36. E. Graugnard, J. S. King, D. P. Gaillot, C. J. Summers, *Adv. Funct. Mater.* **2006**, *16*, 1187.

37. Z. Chen, L. Fang, W. Dong, F. Zheng, M. Shen, J. Wang, *J. Mater. Chem. A* **2014**, *2*, 824.

38. M. Kaneko, I. Okura, *Photocatalysis: Science and Technology*. Springer-Verlag, Berlin, Heidelberg, New York **2002**.

39. K. Ozawa, M. Emori, S. Yamamoto, R. Yukawa, S. Yamamoto, R. Hobara, K. Fujikawa, H. Sakama, I. Matsuda, *J. Phys. Chem. Lett.* **2014**, *5*, 1953.

40. L. Sang, Y. Zhang, J. Wang, Y. Zhao, Y.-t. Chen, *Phys. Chem. Chem. Phys.* **2016**, *18*, 15427.

41. E. S. Kwak, W. Lee, N.-G. Park, J. Kim, H. Lee, *Adv. Funct. Mater.* **2009**, *19*, 1093.

42. H. Chen, S. Chen, X. Quan, Y. Zhang, *Environ. Sci. Technol.* **2010**, *44*, 451.

43. Y. Nosaka, N. Ohta, H. Miyama, *J. Phys. Chem.* **1990**, *94*, 3752.

44. A. J. Hoffman, H. Yee, G. Mills, M. R. Hoffmann, *J. Phys. Chem.* **1992**, *96*, 5540.

45. K. Fujihara, S. Izumi, T. Ohno, M. Matsumura, *J. Photochem. Photobiol. A* **2000**, *132*, 99.

46. T. Cherdhirankorn, M. Retsch, U. Jonas, H.-J. Butt, K. Koynov, *Langmuir* **2010**, *26*, 10141.

47. R. Raccis, A. Nikoubashman, M. Retsch, U. Jonas, K. Koynov, H.-J. Butt, C. N. Likos, G. Fytas, *ACS Nano* **2011**, *5*, 4607.

48. S. Eyderman, S. John, A. Deinega, *J. Appl. Phys.* **2013**, *113*, 154315.

49. N. Hosaka, T. Sekiya, C. Satoko, S. Kurita, *J. Phys. Soc. Jpn.* **1997**, *66*, 877.

50. B. J. Frey, P. Kuang, M.-L. Hsieh, J.-H. Jiang, S. John, S.-Y. Lin, *Sci. Rep.* **2017**, *7*, 4171.

51. V. Likodimos, *Appl. Catal., B* **2018**, *230*, 269.

52. A. Chutinan, S. John, *Phys. Rev. A* **2008**, *78*, 023825.

53. G. Demésy, S. John, *J. Appl. Phys.* **2012**, *112*, 074326.

54. P. Kuang, A. Deinega, M.-L. Hsieh, S. John, S.-Y. Lin, *Opt. Lett.* **2013**, *38*, 4200.

55. X. Zhang, S. John, *Phys. Rev. B* **2019**, *99*, 035417.

56. G. A. Hope, A. J. Bard, *J. Phys. Chem.* **1983**, *87*, 1979.

57. F. Hossein-Babaei, M. M. Lajvardi, N. Alaei-Sheini, *Appl. Phys. Lett.* **2015**, *106*, 083503.

58. P. Kuang, S. Eyderman, M.-L. Hsieh, A. Post, S. John, S.-Y. Lin, *ACS Nano* **2016**, *10*, 6116.

59. A. Mavrokefalos, S. E. Han, S. Yerci, M. S. Branham, G. Chen, *Nano Lett.* **2012**, *12*, 2792.

60. K. Kumar, A. Khalatpour, G. Liu, J. Nogami, N. P. Kherani, *Sol. Energy* **2017**, *155*, 1306.

61. S. Bhattacharya, S. John, *Phys. Rev. Appl.* **2018**, *9*, 044009.

62. S. Eyderman, S. John, M. Hafez, S. S. Al-Ameer, T. S. Al-Harby, Y. Al-Hadeethi, D. M. Bouwes, *J. Appl. Phys.* **2015**, *118*, 023103.

63. N. Hayashi, K. Kato, A. Yamakata, *J. Chem. Phys.* **2020**, *152*, 241101.

64. C. Liu, J. Tang, H. M. Chen, B. Liu, P. Yang, *Nano Lett.* **2013**, *13*, 2989.

SUPPORTING INFORMATION

Additional supporting information may be found online in the Supporting Information section at the end of the article.